

Structured Quantum Optimal Control under Bandwidth and Smoothness Constraints

An Inexact Proximal-ADMM Approach for Low-Complexity Pulse Synthesis

Ziwen Song

Independent Researcher, Datong, Shanxi, China

szw15235225125@gmail.com

March 11, 2026

Abstract

Quantum optimal control is often judged by nominal fidelity alone, even though realistic pulse-design studies must also account for bandwidth, amplitude, and smoothness constraints. I study this structured-control regime with an inexact Proximal-ADMM framework that combines gate-infidelity minimization with L_1 sparsity, total-variation regularization, explicit band-limit projection, and box constraints in a single loop. The method is benchmarked against GRAPE, standard Krotov, and L-BFGS-B on a single-qubit X gate, a leakage-prone qutrit task, and a two-qubit entangling gate. Across ten random seeds, Pareto scans, ablations, filtered-baseline fairness checks, significance analysis with false-discovery-rate correction, and robustness tests, the method is not a universal winner in either nominal fidelity or wall-clock cost. Its value is instead to expose and stabilize a low-complexity frontier of the fidelity–complexity landscape. After retuning the PADMM budgets and warm-start lengths, the qutrit and two-qubit structured fidelities rise to 0.6672 ± 0.0001 and 0.6342 ± 0.0003 , respectively, while preserving markedly lower complexity than unconstrained quasi-Newton solutions. These values remain well below deployment-grade gate thresholds, so the contribution should still be read as a numerical framework for constrained pulse synthesis rather than as a finished route to immediately deployable high-fidelity gates. Training-time robust optimization yields only task-dependent gains, with the clearest effect appearing in qutrit drift robustness and amounting to a small absolute improvement. The results therefore position PADMM as a constraint-native framework for low-complexity frontier exploration, not as a replacement for unconstrained high-fidelity solvers.

1 Introduction

Shaped-field control is central to modern atomic, molecular and optical physics, where it appears in coherent state transfer, spectroscopy, matter-wave manipulation, quantum information processing, and sensing [1, 2, 3, 4, 5]. In all of these settings, the formal task is similar: one specifies a dynamical model and a target transformation, and then optimizes a time-dependent field so that the final evolution approaches the desired operation as closely as possible. Over the last two decades, methods such as GRAPE, Krotov, CRAB, and quasi-Newton optimization have made high-fidelity quantum control a standard numerical tool [6, 7, 8, 9, 10, 11, 12].

In many physically relevant problems, however, the most useful pulse is not the one with the highest nominal fidelity in an unconstrained search space. Fields with excessive spectral content, sharp slice-to-slice variation, or large amplitude excursions are often harder to interpret and harder to relate to realistic pulse-generation hardware [13, 14, 15, 16, 17]. This issue is especially visible in control problems with leakage channels or multilevel structure, where numerically successful solutions may rely on rapidly oscillatory corrections whose physical role is not transparent [18, 19, 20, 21]. A common practical response is to optimize fidelity first and then smooth or filter the resulting pulse afterward. That workflow is often serviceable, but it does not preserve a clean link between the optimization objective and the final waveform that one would actually want to analyse or implement.

The present work explores an alternative viewpoint in which bandwidth limitation, smoothness, and sparsity are incorporated directly into the control problem. The goal is not to surpass unconstrained solvers in the highest-fidelity corner of parameter space, and the resulting structured solutions in the harder qutrit and two-qubit tasks do not yet reach a fidelity regime that would normally be considered deployment-ready. Instead, the goal is to identify whether a constraint-native optimization framework can reproducibly occupy and characterize a useful low-complexity region of the fidelity-complexity landscape. This question is well aligned with the broader AMO tradition of balancing controllability against pulse simplicity and physical interpretability and with the wider control-landscape literature that emphasizes practical restrictions on admissible fields [22, 23, 24, 25, 26, 27].

To address it, I introduce an inexact Proximal-ADMM framework for structured pulse synthesis. The method borrows the variable-splitting logic of proximal and ADMM-type optimization [28, 29, 30, 31, 32, 33, 34], but combines it with adjoint-based fidelity gradients and explicit Fourier-domain band-limit projection in a form suited to quantum control. The naming is deliberate. The control-variable subproblem is not solved exactly at every outer iteration, so the algorithm should be regarded as an inexact ADMM-inspired framework rather than as textbook ADMM. The numerical study below shows that this distinction is not merely terminological: the method is best judged by the part of control space it reaches and stabilizes, not by whether it overtakes unconstrained quasi-Newton solvers in raw nominal fidelity.

2 Model and method

2.1 Discrete-time control model

I consider a closed-system unitary dynamics of the form

$$\dot{U}(t) = -i \left(H_0 + \sum_{m=1}^M u_m(t) H_m \right) U(t), \quad U(0) = I, \quad (1)$$

where H_0 is the drift Hamiltonian, H_m are control Hamiltonians, and $u_m(t)$ are the control amplitudes. After discretizing the total duration T into N equal time slices of size $\Delta t = T/N$ and using a piecewise-constant approximation, the propagation becomes

$$U_{k+1} = \exp \left[-i\Delta t \left(H_0 + \sum_{m=1}^M u_m[k] H_m \right) \right] U_k. \quad (2)$$

Collecting the controls over all channels and time slices yields an optimization variable $\mathbf{u} \in \mathbb{R}^{M \times N}$. This piecewise-constant discretization and gate-synthesis viewpoint follow the standard setup used throughout numerical quantum control [6, 7, 35, 10].

For a target gate U_{tar} , the control objective is measured through the standard gate fidelity

$$F(\mathbf{u}) = \frac{\left| \text{Tr} \left(U_{\text{tar}}^\dagger U_N(\mathbf{u}) \right) \right|^2}{d^2}, \quad (3)$$

and the corresponding smooth loss is $\mathcal{J}_{\text{fid}}(\mathbf{u}) = 1 - F(\mathbf{u})$, where d denotes the Hilbert-space dimension of the controlled unitary.

For the piecewise-constant discretization used here, each slice propagator is

$$U_{k+1} = G_k U_k, \quad G_k = \exp \left[-i\Delta t \left(H_0 + \sum_{m=1}^M u_m[k] H_m \right) \right]. \quad (4)$$

Introducing backward co-states through

$$\Lambda_k = G_k^\dagger \Lambda_{k+1}, \quad \Lambda_N = U_{\text{tar}} \text{Tr} \left(U_{\text{tar}}^\dagger U_N \right)^*, \quad (5)$$

the fidelity gradient takes the familiar adjoint form

$$\frac{\partial \mathcal{J}_{\text{fid}}}{\partial u_m[k]} = -\frac{2\Delta t}{d^2} \text{Im} \left[\text{Tr} \left(\Lambda_{k+1}^\dagger H_m U_{k+1} \right) \right], \quad (6)$$

which is the smooth term used throughout the inner updates.

2.2 Structured pulse objective

The structured-control problem considered here is

$$\min_{\mathbf{u}} \mathcal{J}_{\text{fid}}(\mathbf{u}) + \lambda_1 \|\mathbf{u}\|_1 + \lambda_2 \|D\mathbf{u}\|_1 + \delta_{\mathcal{B}}(\mathbf{u}) + \delta_{\mathcal{A}}(\mathbf{u}), \quad (7)$$

where $\|\mathbf{u}\|_1$ promotes amplitude sparsity, D is the first-order finite-difference operator in time so that $\|D\mathbf{u}\|_1$ is the total-variation penalty, $\delta_{\mathcal{B}}$ is the indicator function of the band-limited admissible set, and $\delta_{\mathcal{A}}$ enforces amplitude box constraints. Here $\delta_{\mathcal{C}}(\cdot)$ is used in the standard optimization sense: it is zero on the admissible set \mathcal{C} and $+\infty$ outside it.

The band-limit constraint is implemented with a Fourier-domain projector. If \mathcal{F} denotes the discrete Fourier transform and \mathcal{M}_{ω_c} is a binary frequency mask that removes components above a cutoff ω_c , then the projector onto the admissible low-bandwidth set is

$$\mathcal{P}_{\mathcal{B}}(\mathbf{x}) = \mathcal{F}^{-1}(\mathcal{M}_{\omega_c} \odot \mathcal{F}(\mathbf{x})). \quad (8)$$

The first-difference operator entering the total-variation term is defined componentwise by

$$(D\mathbf{u})_k = \mathbf{u}_{k+1} - \mathbf{u}_k, \quad (9)$$

so that $\|D\mathbf{u}\|_1$ penalizes abrupt slice-to-slice changes in the pulse envelope. This particular combination of spectral truncation and variation control is motivated by earlier studies on bandwidth-limited and hardware-aware quantum control, but is treated here inside one optimization loop rather than as a post-processing step [16, 17, 36, 37].

2.3 Variable splitting and inexact PADMM updates

To separate the nonsmooth terms, I introduce auxiliary variables

$$\mathbf{z}_1 = \mathbf{u}, \quad \mathbf{z}_2 = D\mathbf{u}, \quad \mathbf{z}_3 = \mathbf{u}, \quad (10)$$

corresponding to sparsity, total variation, and band limitation. For compact notation, I write $\mathbf{z} = (\mathbf{z}_1, \mathbf{z}_2, \mathbf{z}_3)$ and $\mathbf{y} = (\mathbf{y}_1, \mathbf{y}_2, \mathbf{y}_3)$. With scaled dual variables $\mathbf{y}_1, \mathbf{y}_2, \mathbf{y}_3$, the augmented Lagrangian reads

$$\begin{aligned} \mathcal{L}_{\rho}(\mathbf{u}, \mathbf{z}, \mathbf{y}) &= \mathcal{J}_{\text{fid}}(\mathbf{u}) + \delta_{\mathcal{A}}(\mathbf{u}) + \lambda_1 \|\mathbf{z}_1\|_1 + \lambda_2 \|\mathbf{z}_2\|_1 + \delta_{\mathcal{B}}(\mathbf{z}_3) \\ &+ \frac{\rho_1}{2} \|\mathbf{u} - \mathbf{z}_1 + \mathbf{y}_1\|_2^2 + \frac{\rho_2}{2} \|D\mathbf{u} - \mathbf{z}_2 + \mathbf{y}_2\|_2^2 + \frac{\rho_3}{2} \|\mathbf{u} - \mathbf{z}_3 + \mathbf{y}_3\|_2^2 - \sum_{j=1}^3 \frac{\rho_j}{2} \|\mathbf{y}_j\|_2^2. \end{aligned} \quad (11)$$

The key methodological boundary is that the \mathbf{u} subproblem is not solved exactly. Instead, at each outer iteration r the method uses a finite number of inner gradient steps

indexed by s ,

$$\mathbf{u}^{(r,s+1)} = \Pi_{\mathcal{A}}[\mathbf{u}^{(r,s)} - \eta \nabla_{\mathbf{u}} \mathcal{L}_{\rho}(\mathbf{u}^{(r,s)}, \mathbf{z}^{(r)}, \mathbf{y}^{(r)})], \quad (12)$$

where $\Pi_{\mathcal{A}}$ denotes projection onto the amplitude box. The smooth gradient is obtained by the usual forward-backward propagation chain used in adjoint-based gate optimization, and the quadratic penalty terms are accumulated explicitly in control space. In that sense, the method sits between standard first-order proximal splitting and the adjoint-gradient machinery common in quantum control [28, 29, 38, 39, 40].

Writing out the derivative of the augmented Lagrangian makes the update structure explicit:

$$\begin{aligned} \nabla_{\mathbf{u}} \mathcal{L}_{\rho} &= \nabla_{\mathbf{u}} \mathcal{J}_{\text{fid}}(\mathbf{u}) + \rho_1(\mathbf{u} - \mathbf{z}_1 + \mathbf{y}_1) + \rho_2 D^{\top}(D\mathbf{u} - \mathbf{z}_2 + \mathbf{y}_2) \\ &+ \rho_3(\mathbf{u} - \mathbf{z}_3 + \mathbf{y}_3). \end{aligned} \quad (13)$$

Equation (13) shows why the method is algebraically convenient in the present setting: the expensive part remains the fidelity gradient in Eq. (6), while the constraint terms contribute only simple linear operations and projections. That convenience should not be confused with superior runtime. In the present implementation, the efficiency table below shows that PADMM and PADMM-Warm are usually slower than L-BFGS-B and often slower than GRAPE because they require many more inner gradient evaluations. Their value lies in constraint expression and structured search-space navigation, not in raw computational speed. This also clarifies the distinction from quasi-Newton baselines such as BFGS and L-BFGS-B, whose strength lies in curvature modeling rather than explicit nonsmooth splitting [39, 41, 42, 43, 44, 12].

The auxiliary variables are then updated through soft-thresholding and band-limit projection,

$$\mathbf{z}_1^{(r+1)} = \text{soft}_{\lambda_1/\rho_1}(\mathbf{u}^{(r+1)} + \mathbf{y}_1^{(r)}), \quad (14)$$

$$\mathbf{z}_2^{(r+1)} = \text{soft}_{\lambda_2/\rho_2}(D\mathbf{u}^{(r+1)} + \mathbf{y}_2^{(r)}), \quad (15)$$

$$\mathbf{z}_3^{(r+1)} = \mathcal{P}_{\mathcal{B}}(\mathbf{u}^{(r+1)} + \mathbf{y}_3^{(r)}), \quad (16)$$

followed by the scaled dual updates

$$\mathbf{y}_1^{(r+1)} = \mathbf{y}_1^{(r)} + \mathbf{u}^{(r+1)} - \mathbf{z}_1^{(r+1)}, \quad (17)$$

$$\mathbf{y}_2^{(r+1)} = \mathbf{y}_2^{(r)} + D\mathbf{u}^{(r+1)} - \mathbf{z}_2^{(r+1)}, \quad (18)$$

$$\mathbf{y}_3^{(r+1)} = \mathbf{y}_3^{(r)} + \mathbf{u}^{(r+1)} - \mathbf{z}_3^{(r+1)}. \quad (19)$$

Here $\text{soft}_{\tau}(x) = \text{sign}(x) \max(|x| - \tau, 0)$ denotes componentwise soft-thresholding. The \mathbf{z}_1 update therefore enforces amplitude sparsity, the \mathbf{z}_2 update enforces temporal smoothness through sparse increments, and the \mathbf{z}_3 update imposes the explicit band limit in Fourier space. Because the alternating subproblems are not solved exactly, the method is best

described as an inexact Proximal-ADMM framework rather than as strict textbook ADMM. This terminological boundary is important because classical convergence results for ADMM assume stronger control over the subproblem solves than is imposed here [28, 29, 31].

2.4 Warm-starting and robust training

Raw PADMM can be sensitive to initialization, so I also consider a warm-start strategy in which a short GRAPE stage is used to move the controls into a higher-fidelity basin before the structured updates are activated. If $\mathcal{W}_R(\cdot)$ denotes R warm-start steps, the initialization becomes

$$\mathbf{u}^{(0)} = \mathcal{W}_R(\mathbf{u}_{\text{init}}). \quad (20)$$

To probe method boundaries, I additionally examine a training-time robust extension in which the nominal infidelity is replaced by a finite sample-average objective over a small perturbation ensemble. Let \mathcal{S} denote the set of sampled perturbation scenarios and let N_s be the number of samples in that ensemble. The robust objective is then written as

$$\mathcal{J}_{\text{rob}}(\mathbf{u}) = \frac{1}{N_s} \sum_{s \in \mathcal{S}} \mathcal{J}_{\text{fid}}(\mathbf{u}; s), \quad (21)$$

where \mathcal{S} contains nominal dynamics together with detuning, amplitude-error, and control-drift scenarios. This mirrors the broader robust-control perspective in quantum technology, where one is often interested in stability under calibrated uncertainty rather than in a single nominal optimum [45, 46, 4]. Its gradient keeps the same averaging structure,

$$\nabla \mathcal{J}_{\text{rob}}(\mathbf{u}) = \frac{1}{N_s} \sum_{s \in \mathcal{S}} \nabla \mathcal{J}_{\text{fid}}(\mathbf{u}; s), \quad (22)$$

so the robust variant changes the cost of each inner step mainly through repeated forward-backward propagations over the perturbation ensemble rather than through any modification of the proximal updates themselves.

3 Numerical experiments

The numerical study uses three simulated pulse-synthesis tasks: a single-qubit X gate, a leakage-prone qutrit control problem, and a two-qubit entangling gate. Although simplified, these models span three control situations that are representative for structured pulse design: a low-dimensional reference problem, a multilevel problem in which leakage and spectral content are strongly coupled, and a modestly larger gate-synthesis task in which unconstrained high-fidelity solutions become structurally complicated. The benchmark includes GRAPE, standard Krotov implemented through `qucontrol/krotov`, L-BFGS-B, PADMM, and PADMM-Warm [7, 47, 48, 11]. Ten random seeds {3, 7, 11, 19, 23, 29, 31, 37, 41, 43} are used for the principal multiseed statistics. In addition to nominal fidelity, I report bandwidth

excess, total variation, wall-clock time, objective-evaluation counts, and gradient-evaluation counts. Post-training robustness is evaluated under detuning, amplitude miscalibration, and control drift. For readability, the main plots use standard errors across seeds as error bars, whereas the tables report the full standard deviations and 95% confidence intervals are quoted in the significance analysis.

3.1 Reproducibility protocol

Task	Hamiltonian summary	T	N	Δt	Channels	u_{\max}	init. scale
1Q X gate	$H_0 = \frac{0.2}{2}\sigma_z, H_x, H_y$ drives	4.80	40	0.12	2	4.00	0.020
Qutrit leakage	$\omega_{01} = 1.0, \alpha = -0.22$, quadrature drives	4.80	60	0.08	2	2.80	0.015
2Q entangler	$\omega_1 = 0.3, \omega_2 = 0.36, J = 0.15$	3.20	40	0.08	3	3.20	0.010

Table 1: Task-level reproducibility details used in all numerical experiments.

Task	Classical baselines	PADMM hyperparameters	Warm start	Robust ensemble
1Q X gate	Fixed 120 iterations; $\lambda_a = 0.25$, Fixed 40 iterations; SciPy L-BFGS-B convergence or max 80 iterations	$\lambda_1 = 0.0005, \lambda_{TV} = 0.0008, \rho_1 = \rho_{TV} = \rho_{BW} = 1.0, \omega_c = 1.8, \eta = 0.04$, inner=6, outer=120	GRAPE warm start $R = 25$ then PADMM	$N_s = 6$; detuning fractions [0.05]; amplitude errors [-0.05, 0.05]; drift strengths [0.02]
Qutrit leakage	Fixed 180 iterations; $\lambda_a = 12.0$, Fixed 40 iterations; SciPy L-BFGS-B convergence or max 120 iterations	$\lambda_1 = 0.0001, \lambda_{TV} = 0.0001, \rho_1 = \rho_{TV} = \rho_{BW} = 1.0, \omega_c = 2.5, \eta = 0.05$, inner=8, outer=220	GRAPE warm start $R = 40$ then PADMM	$N_s = 6$; detuning fractions [0.05]; amplitude errors [-0.05, 0.05]; drift strengths [0.02]
2Q entangler	Fixed 80 iterations; $\lambda_a = 10.0$, Fixed 40 iterations; SciPy L-BFGS-B convergence or max 60 iterations	$\lambda_1 = 0.001, \lambda_{TV} = 0.0012, \rho_1 = \rho_{TV} = \rho_{BW} = 1.0, \omega_c = 1.0, \eta = 0.03$, inner=4, outer=80	GRAPE warm start $R = 25$ then PADMM	$N_s = 6$; detuning fractions [0.05]; amplitude errors [-0.05, 0.05]; drift strengths [0.02]

Table 2: Optimizer hyperparameters, stopping budgets, and robust-training settings.

Tables 1 and 2 collect the task definitions and optimizer settings needed to reproduce the reported experiments. In particular, they specify the task Hamiltonians, total durations,

Table 3: Multi-seed benchmark statistics. Fidelity is reported as mean \pm standard deviation together with the median and the best observed value. Complexity metrics are computed with respect to the PADMM reference bandwidth for each task.

Task	Method	Fidelity ($\mu \pm \sigma$)	Median	Best	Total Variation ($\mu \pm \sigma$)
1Q-X	GRAPE	0.7491 ± 0.3466	0.9353	0.9971	1.781 ± 0.232
	Krotov	0.6456 ± 0.3289	0.6706	0.9932	18.465 ± 4.715
	L-BFGS-B	1.0000 ± 0.0000	1.0000	1.0000	2.958 ± 2.410
	PADMM	0.6306 ± 0.3810	0.7930	0.9936	0.748 ± 0.381
	PADMM-Warm	0.8741 ± 0.2722	0.9912	0.9995	1.043 ± 0.300
Qutrit-X	GRAPE	0.1416 ± 0.0026	0.1418	0.1457	2.045 ± 0.210
	Krotov	0.1111 ± 0.0005	0.1111	0.1119	25.897 ± 6.334
	L-BFGS-B	0.9401 ± 0.0420	0.9512	0.9956	79.184 ± 10.517
	PADMM	0.6663 ± 0.0001	0.6663	0.6665	5.952 ± 0.029
	PADMM-Warm	0.6672 ± 0.0001	0.6672	0.6673	5.977 ± 0.032
2Q-Ent	GRAPE	0.5137 ± 0.0009	0.5136	0.5159	2.195 ± 0.143
	Krotov	0.5781 ± 0.0006	0.5781	0.5794	23.797 ± 4.236
	L-BFGS-B	0.9998 ± 0.0001	0.9999	1.0000	41.675 ± 6.541
	PADMM	0.6255 ± 0.0003	0.6255	0.6259	0.523 ± 0.010
	PADMM-Warm	0.6342 ± 0.0003	0.6341	0.6345	0.731 ± 0.011

discretization steps, control-channel counts, amplitude bounds, cutoff frequencies, regularization weights, penalty parameters, learning rates, inner-loop lengths, warm-start budgets, and the perturbation ensemble used in the training-time robust study. The stopping rules are iteration-budget based for GRAPE, Krotov, and the PADMM family, while L-BFGS-B uses the native SciPy convergence test subject to the stated maximum iteration budget.

Table 4: Efficiency statistics across seeds. Wall-clock time is measured in seconds. For standard Krotov, gradient evaluations are reported as zero because the implementation uses the native iterative update rule rather than explicit gradient calls.

Task	Method	Wall-clock ($\mu \pm \sigma$)	Objective Evals ($\mu \pm \sigma$)	Gradient Evals ($\mu \pm \sigma$)
1Q-X	GRAPE	1.53 ± 0.02	241.0 ± 0.0	120.0 ± 0.0
	Krotov	21.01 ± 0.44	41.0 ± 0.0	0.0 ± 0.0
	L-BFGS-B	0.26 ± 0.09	40.8 ± 13.5	39.8 ± 13.5
	PADMM	5.18 ± 0.08	840.0 ± 0.0	720.0 ± 0.0
	PADMM-Warm	5.49 ± 0.09	891.0 ± 0.0	745.0 ± 0.0
Qutrit-X	GRAPE	3.10 ± 0.07	361.0 ± 0.0	180.0 ± 0.0
	Krotov	47.06 ± 0.27	41.0 ± 0.0	0.0 ± 0.0
	L-BFGS-B	2.66 ± 0.30	288.6 ± 29.8	287.6 ± 29.8
	PADMM	42.54 ± 0.50	4840.0 ± 0.0	4400.0 ± 0.0
	PADMM-Warm	44.51 ± 0.25	5081.0 ± 0.0	4520.0 ± 0.0
2Q-Ent	GRAPE	2.48 ± 0.07	161.0 ± 0.0	80.0 ± 0.0
	Krotov	44.41 ± 0.31	41.0 ± 0.0	0.0 ± 0.0
	L-BFGS-B	2.19 ± 0.12	138.0 ± 8.0	137.0 ± 8.0
	PADMM	17.73 ± 0.38	1120.0 ± 0.0	960.0 ± 0.0
	PADMM-Warm	20.32 ± 0.19	1281.0 ± 0.0	1040.0 ± 0.0

3.2 Main benchmark

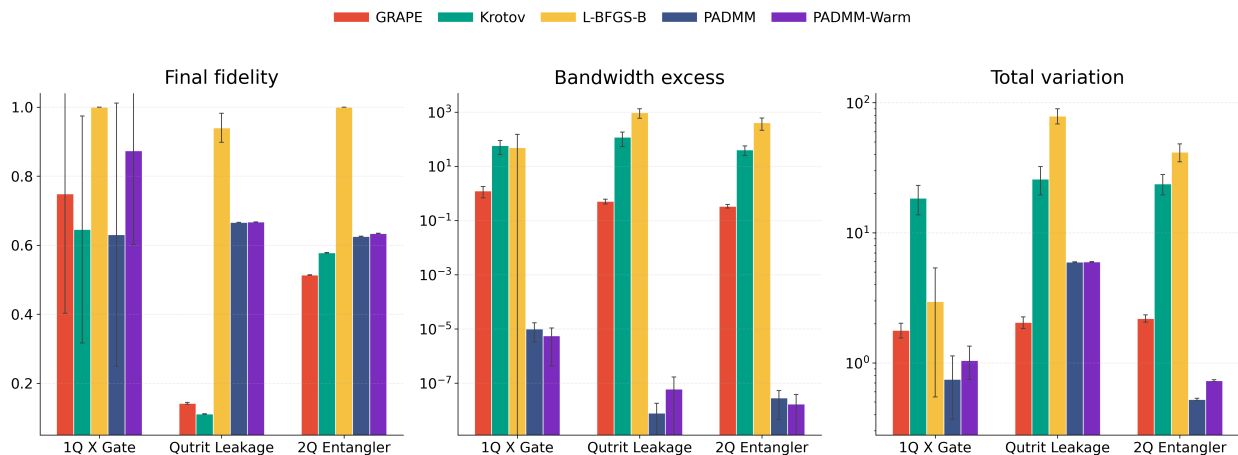


Figure 1: Main benchmark summary. Panels show ten-seed means for (a) nominal fidelity, (b) bandwidth excess, and (c) total variation across the five baseline methods. Error bars denote standard errors across seeds; full standard deviations are listed in the benchmark table.

The main benchmark shows a clear division of roles among the methods. L-BFGS-B remains the strongest nominal-fidelity solver, especially in the single-qubit and two-qubit tasks. However, this performance is accompanied by substantially larger structural complexity. In the qutrit task, for example, L-BFGS-B reaches a mean fidelity of 0.9401 ± 0.0420 with a total variation of about 79.18, whereas the PADMM family stays near total-variation values

of order 5. The central comparison is therefore not “best fidelity” versus “worse fidelity” in isolation, but rather where each method lives in the fidelity-complexity landscape.

Retuning the PADMM budget materially improves the structured part of the benchmark. In the single-qubit task, PADMM-Warm still gives the clearest but also the noisiest boost, with the mean fidelity increasing from 0.6306 for PADMM to 0.8741. In the qutrit and two-qubit tasks, the updated PADMM family now reaches 0.6663/0.6672 and 0.6255/0.6342 for PADMM/PADMM-Warm, respectively. In the qutrit task the extra gain from warm-starting becomes small once the PADMM inner budget is increased, whereas in the two-qubit task warm-starting still gives a visible upward shift. Even after this retuning, however, the structured fidelities in the harder tasks remain modest in absolute terms. They therefore support a claim about constrained frontier exploration and low-complexity pulse synthesis, not a claim about immediately usable high-fidelity gate control.

3.3 Pareto scans, ablations, and sensitivity

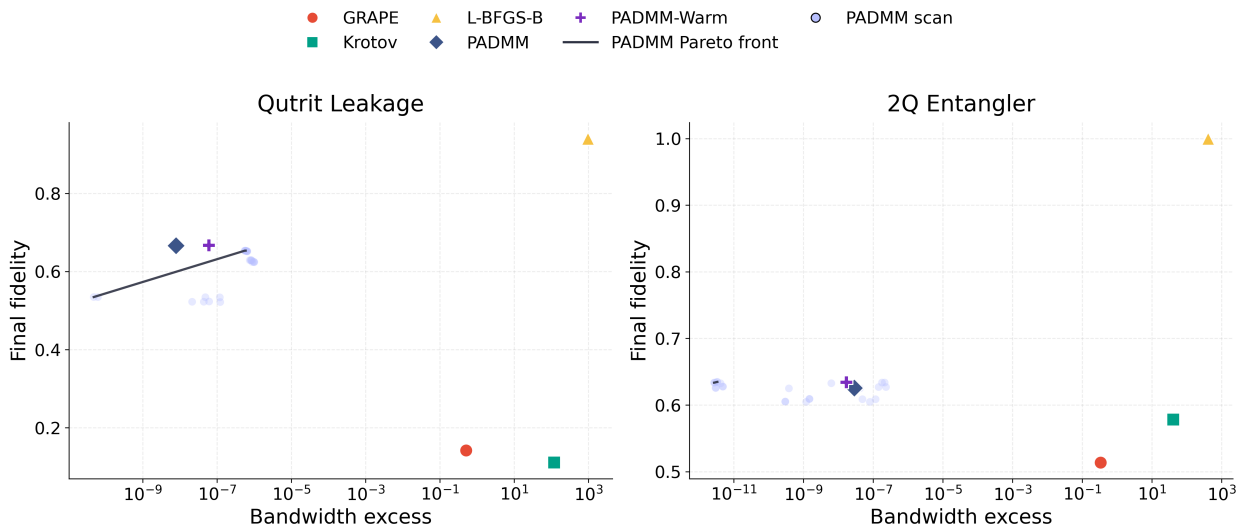


Figure 2: Fidelity-complexity Pareto fronts. Panels show the qutrit and two-qubit tasks; pale points denote scanned PADMM configurations, the dark curve marks the non-dominated front, and colored symbols indicate baseline methods.

Table 5: Constraint-component ablation of PADMM.

Task	Variant	Fidelity	Bandwidth Excess	Total Variation
1Q-X	full	0.9936	$2.10e - 06$	1.191
	l1-only	0.9984	$1.53e + 00$	1.486
	tv-only	0.9998	$1.24e + 00$	0.694
	bandlimit-only	0.9991	$2.29e - 07$	1.447
	no-constraints	0.9998	$1.63e + 00$	1.670
Qutrit-X	full	0.6426	$8.27e - 07$	5.136
	l1-only	0.6590	$2.30e + 00$	5.791
	tv-only	0.6622	$1.95e + 00$	5.791
	bandlimit-only	0.6595	$1.82e - 07$	5.669
	no-constraints	0.6622	$2.49e + 00$	5.952
2Q-Ent	full	0.4927	$1.55e - 06$	0.138
	l1-only	0.5002	$9.65e - 02$	0.931
	tv-only	0.5138	$2.15e - 02$	0.304
	bandlimit-only	0.5066	$1.24e - 05$	0.319
	no-constraints	0.5140	$3.28e - 01$	2.243

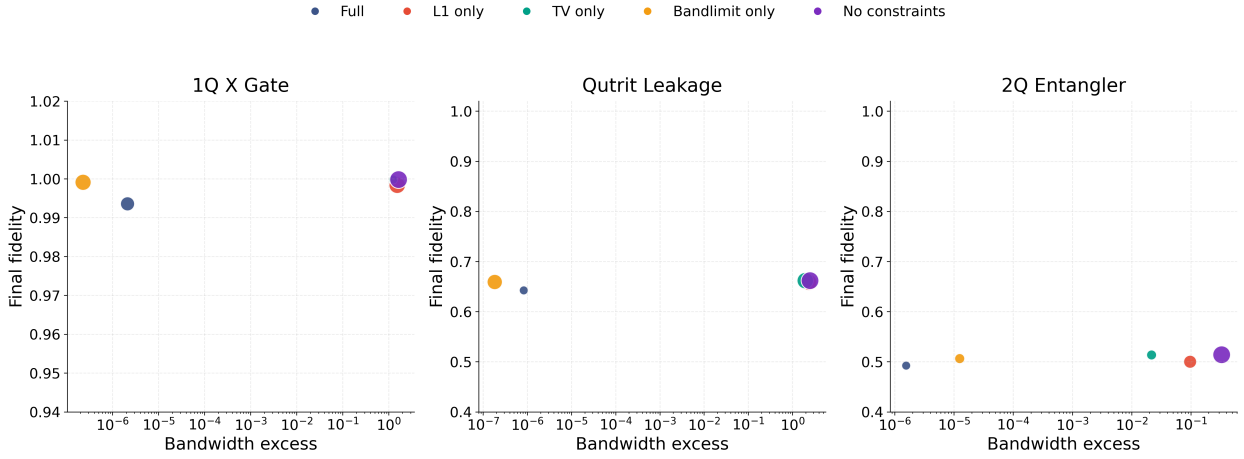


Figure 3: Constraint-component ablation of PADMM. Panels (a)-(c) correspond to the single-qubit, qutrit, and two-qubit tasks. Marker position encodes bandwidth excess and final fidelity, while marker area scales with total variation.

Table 6: Selected PADMM sensitivity results for the qutrit and two-qubit tasks.

Task	Variant	Fidelity	Bandwidth Excess	Total Variation
Qutrit-X	rho-scale=0.5	0.6589	$1.17e - 06$	5.607
	learning-rate=0.0625	0.6577	$7.68e - 07$	5.528
	inner-steps=10	0.6573	$7.36e - 07$	5.512
	rho-scale=1.0	0.6426	$8.27e - 07$	5.136
	learning-rate=0.0500	0.6426	$8.27e - 07$	5.136
	inner-steps=8	0.6426	$8.27e - 07$	5.136
2Q-Ent	inner-steps=6	0.5474	$1.61e - 07$	0.200
	learning-rate=0.0375	0.5249	$2.43e - 07$	0.170
	rho-scale=0.5	0.5000	$7.58e - 05$	0.149
	rho-scale=1.0	0.4927	$1.55e - 06$	0.138
	learning-rate=0.0300	0.4927	$1.55e - 06$	0.138
	inner-steps=4	0.4927	$1.55e - 06$	0.138

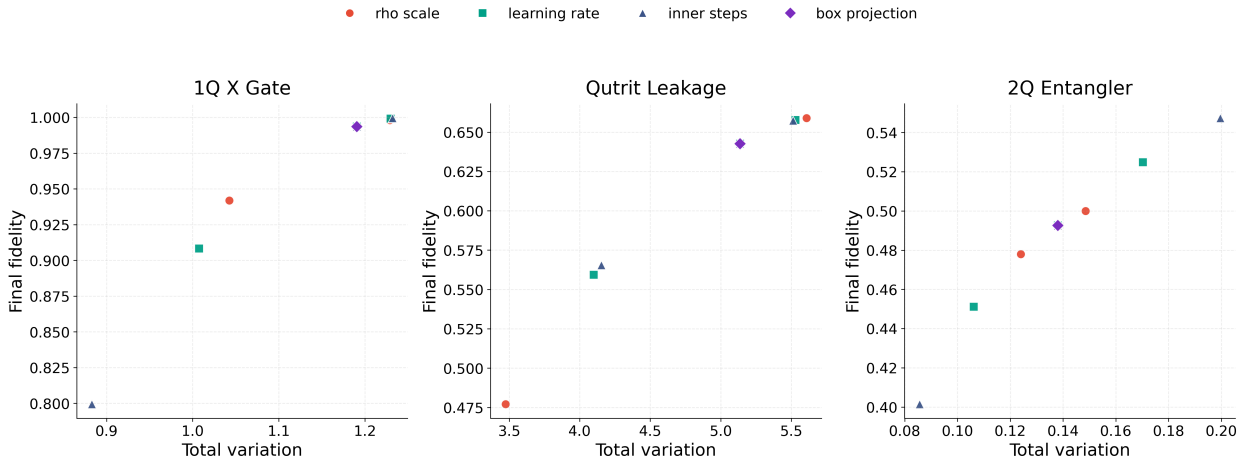


Figure 4: Selected PADMM sensitivity scans. Panels (a)-(c) correspond to the single-qubit, qutrit, and two-qubit tasks, while symbol color and shape indicate the hyperparameter family being varied.

The Pareto scans reinforce the main physical interpretation of the method. PADMM is not competitive in the extreme high-fidelity corner occupied by unconstrained quasi-Newton optimization, but it forms a visible front in the low-complexity region, especially for the qutrit and two-qubit tasks. The ablation study shows that this behaviour is not produced by any single regularizer alone. Removing one structural ingredient can slightly improve nominal fidelity, but it often does so at the expense of much larger bandwidth excess or total variation. The sensitivity scans show that warm-starting and moderate penalty tuning are more important than very fine hyperparameter adjustment. Empirically, the present coarse scans suggest favorable windows of roughly $\rho \in [0.5, 1.0]$, $\eta \in [0.05, 0.0625]$, and 10 outer-gradient inner steps for the qutrit task, and $\eta \in [0.0375, 0.045]$ with 6 inner steps for the two-qubit task, while the acceptable ρ range in the two-qubit case depends more strongly on

how one weighs fidelity against bandwidth excess. These are descriptive windows rather than guarantees, but they make the method’s practical stability region more concrete. In that respect the results resonate with earlier observations that bandwidth restriction and control parameterization can significantly reshape the accessible optimization landscape [9, 16, 24].

3.4 Fairness checks against filtered baselines

Task	Method	Fidelity mean	95% CI	Bandwidth excess	Total variation
Qutrit	grape-filtered	0.1409	[0.1393, 0.1424]	0.0191	0.876
Qutrit	lbfgsb-filtered	0.8787	[0.8528, 0.9046]	23.6	67.121
2Q	grape-filtered	0.5119	[0.5113, 0.5125]	0.107	0.429
2Q	lbfgsb-filtered	0.9868	[0.9788, 0.9947]	26.7	31.616

Table 7: Fairness check using post-processed band-limited baselines. The filtered baselines apply the same bandwidth cutoff used by PADMM, followed by box projection and mild smoothing.

Because the central claim of this paper concerns constraint-native optimization, it is important to check that the reported advantage is not only a consequence of comparing against fully unconstrained baselines. Table 7 therefore reports two post-processed fairness baselines in which the GRAPE and L-BFGS-B solutions are passed through the same band-limit projector used by PADMM, followed by box projection and mild smoothing. This is still not equivalent to optimizing in a shared constrained parameterization, but it is a stricter comparison than evaluating only raw unconstrained pulses. The resulting data show that post-processing can indeed reduce bandwidth excess and total variation, but it does not erase the main fidelity-complexity distinction. In the qutrit task, for example, filtered L-BFGS-B still retains far larger bandwidth excess and total variation than PADMM-Warm, even after the filter stage.

Table 8: Robustness benchmark under detuning, amplitude miscalibration, and control drift. Each entry reports the mean perturbed fidelity across ten random seeds and multiple perturbation levels.

Task	Method	Nominal	Detuning	Amplitude Error	Control Drift
1Q-X	GRAPE	0.7491	0.7487	0.7417	0.7269
	Krotov	0.6456	0.6454	0.6357	0.6285
	L-BFGS-B	1.0000	0.9995	0.9302	0.9752
	PADMM	0.6306	0.6303	0.6253	0.6019
	PADMM-Warm	0.8741	0.8736	0.8634	0.8515
Qutrit-X	GRAPE	0.1416	0.1380	0.1418	0.1570
	Krotov	0.1111	0.1111	0.1111	0.1167
	L-BFGS-B	0.9401	0.8978	0.9067	0.9304
	PADMM	0.6407	0.5979	0.6321	0.6186
	PADMM-Warm	0.6521	0.6093	0.6425	0.6294
2Q-Ent	GRAPE	0.5137	0.5136	0.5133	0.5127
	Krotov	0.5781	0.5779	0.5774	0.5758
	L-BFGS-B	0.9998	0.9998	0.9853	0.9857
	PADMM	0.4922	0.4921	0.4919	0.4915
	PADMM-Warm	0.5406	0.5404	0.5400	0.5393

3.5 Post-training robustness and robust optimization

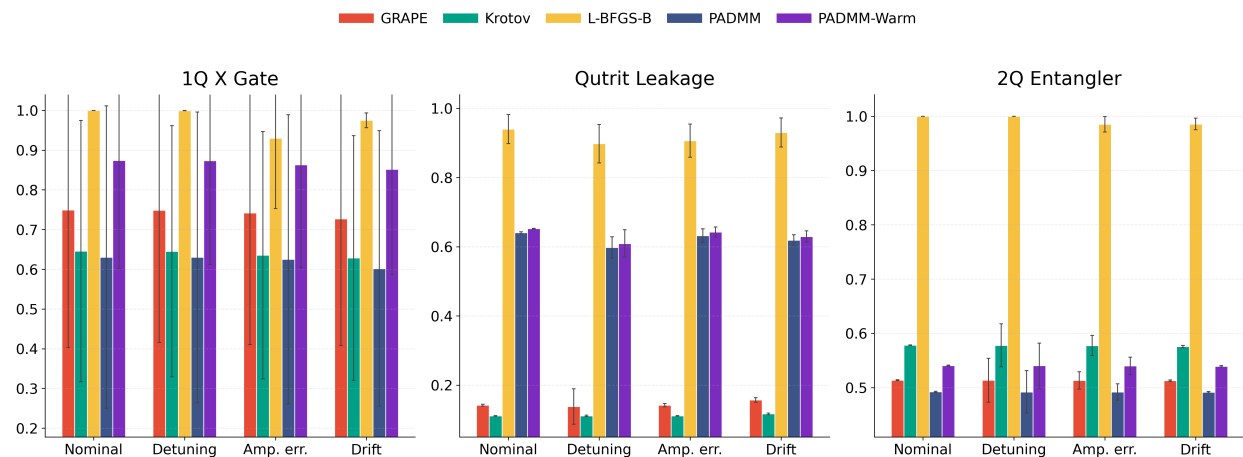


Figure 5: Post-training robustness benchmark. Panels (a)-(c) correspond to the single-qubit, qutrit, and two-qubit tasks and show ten-seed mean fidelities under nominal dynamics, detuning, amplitude error, and control drift. Error bars denote standard errors across seeds.

Even without explicitly training on a robust objective, the structured pulses already display a useful form of passive robustness. PADMM-Warm consistently improves upon PADMM in the post-training robustness tests, which suggests that smoother and spectrally sim-

Table 9: Training-time robust optimization results for the PADMM family. Nominal fidelity and complexity are measured after optimization; detuning and drift columns report post-training robustness means.

Task	Method	Nominal Fidelity	Detuning	Drift	Total Variation
Qutrit-X	PADMM-Warm	0.6521	0.6093	0.6294	5.405
	PADMM-Warm-Robust	0.6517	0.6090	0.6324	5.391
2Q-Ent	PADMM-Warm	0.5406	0.5404	0.5393	0.189
	PADMM-Warm-Robust	0.5405	0.5403	0.5391	0.188

pler controls are less sensitive to moderate model mismatch. This is physically plausible: low-complexity pulses tend to avoid relying on narrow cancellation effects that are easily disrupted by perturbations. Similar robustness-through-structure ideas have appeared in hardware-calibrated and hybrid-control settings, although not in the present proximal-splitting form [26, 27, 49].

Comparison	Task	$\Delta\mu$	95% CI for $\Delta\mu$	Hedges g	Welch p	BH q
PADMM-Warm – PADMM	1Q	0.2435	[-0.0467, 0.5337]	0.70	0.119	0.179
PADMM-Warm – PADMM	Qutrit	0.0009	[0.0008, 0.0009]	9.34	2.15e-14	6.46e-14
PADMM-Warm – PADMM	2Q	0.0087	[0.0084, 0.0089]	26.86	2.01e-22	1.2e-21
Warm-Robust – Warm drift	1Q	0.0580	[-0.1319, 0.2479]	0.26	0.559	0.671
Warm-Robust – Warm drift	Qutrit	0.0030	[0.0019, 0.0040]	2.32	3.87e-05	7.74e-05
Warm-Robust – Warm drift	2Q	-0.0001	[-0.0008, 0.0005]	-0.16	0.713	0.713

Table 10: Selected significance checks with effect sizes and Benjamini–Hochberg false-discovery-rate correction across all six reported comparisons. For the robust-training rows, the compared quantity is the post-training mean fidelity under control drift.

Task	Method	Fidelity ($\mu \pm \sigma$)	Final primal ($\mu \pm \sigma$)	Final dual ($\mu \pm \sigma$)	Final violation ($\mu \pm \sigma$)
1Q	padmm	0.6306±0.3810	6.900e-04±2.4e-04	6.009e-02±3.0e-02	3.644e-04±1.4e-04
1Q	padmm-warm	0.8741±0.2722	4.789e-04±2.8e-04	3.251e-02±3.0e-02	2.517e-04±1.8e-04
Qutrit	padmm	0.6663±0.0001	3.005e-05±3.6e-05	3.607e-03±1.2e-05	2.555e-05±3.6e-05
Qutrit	padmm-warm	0.6672±0.0001	3.536e-05±3.3e-05	3.484e-03±1.2e-05	2.465e-05±2.5e-05
2Q	padmm	0.6255±0.0003	3.999e-05±2.2e-05	8.518e-03±2.1e-05	2.330e-05±1.2e-05
2Q	padmm-warm	0.6342±0.0003	2.393e-05±2.7e-05	6.441e-03±1.1e-05	1.376e-05±1.5e-05

Table 11: Cross-seed PADMM residual diagnostics aggregated over the ten multiseed runs. The values summarize the final primal residual, final dual residual, and final split-constraint violation recorded at the end of optimization.

Task	Hyperparameter	Empirical stable window	Notes
Qutrit	rho-scale	rho_scale=0.5, rho_scale=1.0	higher ρ degrades fidelity noticeably
	learning-rate	learning_rate=0.0500, learning_rate=0.0625	below 0.05 the method under-updates
	inner-steps	inner_steps=8, inner_steps=10	6 steps is visibly worse than 8–10
2Q	rho-scale	rho_scale=0.5, rho_scale=1.0	window depends on whether bandwidth or fidelity is prioritized
	learning-rate	learning_rate=0.0300, learning_rate=0.0375	0.0375 gives the best scanned fidelity
	inner-steps	inner_steps=4, inner_steps=6	more than 4 steps helps, but increases cost

Table 12: Empirical PADMM stability windows inferred from the coarse sensitivity scans. These windows are descriptive rather than exhaustive and indicate settings that remain near the favorable fidelity–complexity region in the current experiments.

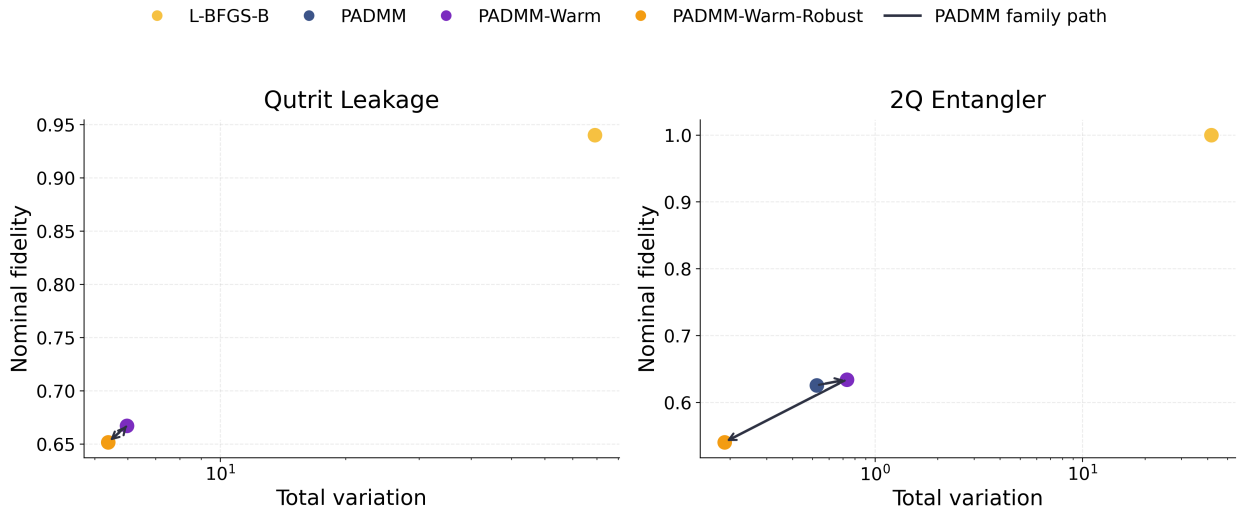


Figure 6: Trade-off trajectory within the PADMM family. Panel (a) shows the qutrit task and panel (b) the two-qubit task. PADMM-Warm moves the method upward in nominal fidelity at a modest complexity cost, while robust training produces only task-dependent adjustments.

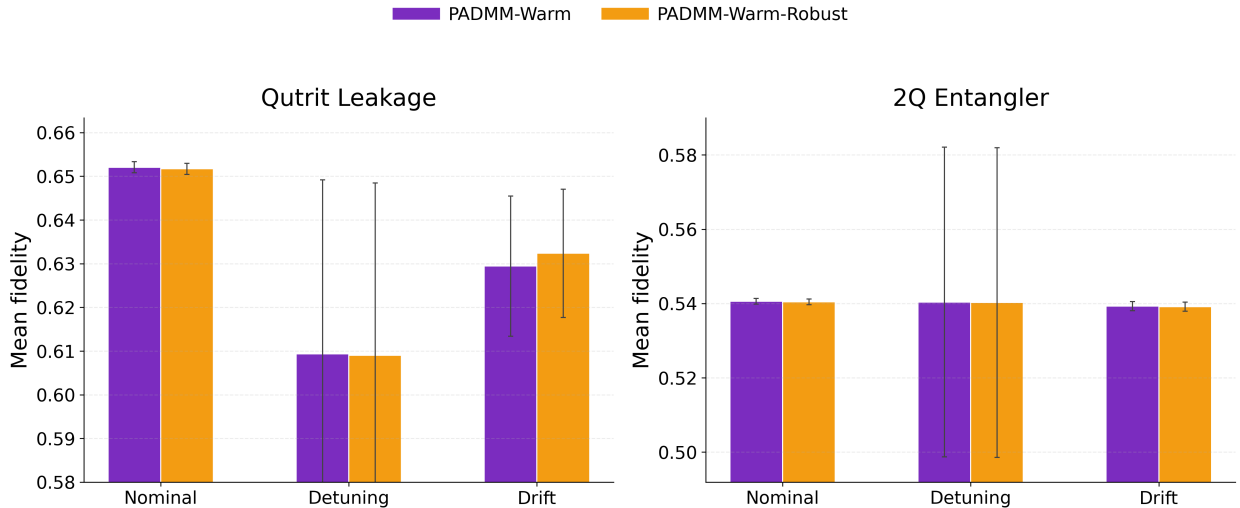


Figure 7: Training-time robust optimization within the PADMM family. Panel (a) shows the qutrit task and panel (b) the two-qubit task. Error bars denote standard errors across seeds. The clearest gain appears in qutrit drift robustness, whereas the two-qubit task is nearly neutral.

The training-time robust optimization study further clarifies the boundary of the method. In the qutrit task, PADMM-Warm-Robust preserves the nominal fidelity almost exactly while slightly improving mean fidelity under control drift, from 0.6294 to 0.6324. The significance table shows that this difference survives Welch testing and false-discovery-rate correction, but the absolute gain is only about 3×10^{-3} . It should therefore be interpreted as a detectable but physically modest effect rather than as a large robustness breakthrough. In the two-qubit task the robust objective is essentially neutral, and in the single-qubit task stronger robust training remains too variable to support a strong claim. This mixed outcome is still informative. It indicates that much of the robustness gain in the PADMM family already originates from pulse structure itself, while explicit robust training becomes useful only when the sampled perturbations align with the dominant failure channels of the control problem.

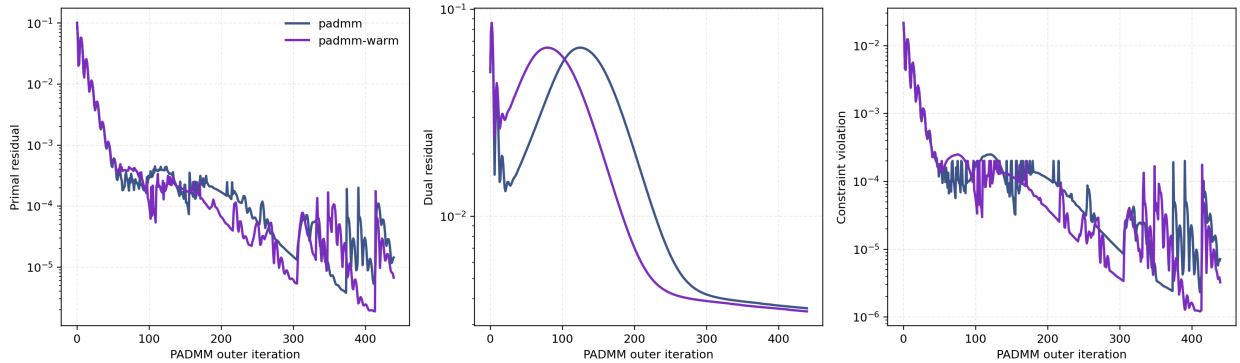


Figure 8: Representative PADMM residual diagnostics for the qutrit task. The plotted quantities are the primal residual, dual residual, and maximum split-constraint violation for PADMM and PADMM-Warm at the default qutrit seed.

The residual diagnostics provide a numerical stability check for the inexact PADMM formulation, but they should still be read as diagnostics rather than as a substitute for theory. The cross-seed diagnostic table shows that the final split-constraint violation remains around the 10^{-4} level or below on average, and that PADMM-Warm generally lowers both the primal and dual residuals in the qutrit task. At the same time, no formal convergence theorem is claimed, the inner-solve error is not adaptively controlled, and the stability windows in the sensitivity scans are empirical rather than exhaustive. The present evidence therefore supports a statement of repeatable numerical behavior, not a statement of guaranteed convergence.

4 Discussion

The most appropriate interpretation of these results is not that PADMM should replace unconstrained high-fidelity solvers. That would be an overstatement. The contribution is narrower and therefore more credible: an inexact Proximal-ADMM framework can serve as a reproducible numerical tool for exploring and stabilizing the low-complexity region of quantum-control pulse space. In that regime, it consistently produces pulses with much smaller bandwidth excess and total variation than L-BFGS-B while retaining moderate fidelity. After retuning, the qutrit and two-qubit structured fidelities do improve noticeably relative to the earlier draft, but they still remain far below the fidelity levels that would usually be treated as deployment-ready quantum gates. The present contribution is therefore a study of constrained frontier structure and optimizer behavior, not a claim that the reported pulses are already physically deployable. This conclusion is consistent with the broader algorithmic lesson of the quantum-control literature: the “best” solver depends strongly on whether the scientific objective is raw fidelity, interpretability, closed-loop adaptability, or robustness under realistic restrictions [10, 25, 48, 50].

For AMO-style control problems, this conclusion matters because pulse simplicity is of-

ten valuable in its own right. Smooth, band-limited fields are easier to interpret, easier to compare across physical scenarios, and more naturally connected to experimentally meaningful pulse shaping. The qutrit example makes this point most clearly: once leakage and spectral content become entangled, the difference between “highest fidelity” and “most useful low-complexity pulse” becomes physically significant rather than merely aesthetic. The observation also aligns with recent pulse-shape studies in atomic interferometry and multi-level gate design, where waveform structure itself strongly influences performance metrics [18, 19, 51]. The filtered-baseline fairness checks sharpen this interpretation: even when unconstrained baselines are post-processed with the same cutoff used by PADMM, they do not collapse onto the same low-complexity operating region. Even so, a stricter comparison based on a shared constrained parameterization for all methods would be preferable in a future follow-up.

The present study is entirely numerical, and that sets a natural boundary on the claims. First, the fairness analysis is stronger than the original unconstrained comparison, but it is still not the strictest possible benchmark: a shared constrained parameterization for all methods would be an even harder test. Second, the PADMM contribution remains primarily algorithmic and numerical rather than theoretical. The residual diagnostics and empirical stability windows show repeatable behavior across seeds and coarse hyperparameter scans, but they do not substitute for a formal convergence result or for an adaptive inner-solve accuracy analysis. Third, the efficiency data do not support marketing PADMM as a faster solver than L-BFGS-B or GRAPE; the attraction of the method is its native handling of nonsmooth structure. Fourth, the statistically meaningful gains of robust training are confined to part of the benchmark, most clearly the qutrit drift scenario, and even there the absolute effect is small. Statistical detectability should therefore not be conflated with large physical impact. Closing the remaining gap to deployment-grade fidelities will likely require more than simply lengthening the present runs. Promising directions include continuation schemes that gradually tighten structural constraints, adaptive updates of ρ and inner-solve accuracy, richer low-bandwidth parameterizations, hybrid warm starts that preserve low-complexity structure more effectively than plain GRAPE, and platform-specific robust objectives that target the dominant leakage and drift channels. Future work should therefore test the same structured-control ideas in open-system settings, in more realistic hardware-transfer models, and in control tasks where the perturbation ensemble can be tied more directly to a particular experimental platform. Natural extensions include open-system optimization, hybrid model-experiment loops, shared constrained parameterizations across baselines, stronger multiple-comparison-aware robustness studies, and learning-assisted structured control [46, 26, 49, 50]. Nevertheless, the current results already support a practical message: if pulse structure is part of the physics question, then it should be part of the optimization problem from the start.

5 Conclusion

I have introduced and benchmarked an inexact Proximal-ADMM approach for structured quantum optimal control under explicit bandwidth, sparsity, and smoothness constraints. Across three simulated pulse-synthesis tasks, the method consistently occupies a low-complexity control regime. After retuning the PADMM budgets and warm-start lengths, the qutrit and two-qubit structured fidelities improve to approximately 0.667 and 0.634, respectively, while training-time robust optimization still provides only modest, task-dependent gains. These outcomes in turn highlight that structured regularization itself is already a major source of passive robustness.

Taken together, these results support a clear role for PADMM in quantum control: not as a universal high-fidelity or high-speed optimizer, and not yet as a route to deployment-grade multilevel gate synthesis, but as a constraint-native numerical framework for low-complexity pulse synthesis and fidelity–complexity frontier exploration. That role makes it a plausible starting point for future studies of physically interpretable control fields in atomic, molecular, optical, and quantum-technology settings.

Data availability

The processed numerical results and configuration files needed to reproduce the figures and tables in this study are available from the author upon reasonable request.

Code availability

The simulation code used to generate the reported results is available from the author upon reasonable request. A cleaned archival release can be prepared for editors and referees if required during review.

References

- [1] Herschel Rabitz, Regina de Vivie-Riedle, Marcus Motzkus, and Karl Kompa. Whither the future of controlling quantum phenomena? *Science*, 288(5467):824–828, 2000.
- [2] Jan Werschnik and E. K. U. Gross. Quantum optimal control theory. *Journal of Physics B: Atomic, Molecular and Optical Physics*, 40(18):R175–R211, 2007.
- [3] Constantin Brif, Raj Chakrabarti, and Herschel Rabitz. Control of quantum phenomena: Past, present and future. *New Journal of Physics*, 12:075008, 2010.
- [4] Steffen J. Glaser, Ugo Boscain, Tommaso Calarco, Christiane P. Koch, Wilfred Köckenberger, Ronnie Kosloff, Ilya Kuprov, Burkhard Luy, Sophie Schirmer, Thomas

- Schulte-Herbrüggen, Dominique Sugny, and Frank K. Wilhelm. Training schrödinger's cat: Quantum optimal control. *The European Physical Journal D*, 69:279, 2015.
- [5] Domenico D'Alessandro. *Introduction to Quantum Control and Dynamics*. Chapman and Hall/CRC, 2008.
- [6] José P. Palao and Ronnie Kosloff. Optimal control theory for unitary transformations. *Physical Review A*, 68:062308, 2003.
- [7] Navin Khaneja, Timo Reiss, Cindie Kehlet, Thomas Schulte-Herbrüggen, and Steffen J. Glaser. Optimal control of coupled spin dynamics: Design of NMR pulse sequences by gradient ascent algorithms. *Journal of Magnetic Resonance*, 172(2):296–305, 2005.
- [8] Wei Zhu, J. Botina, and Herschel Rabitz. Rapidly convergent iteration methods for quantum optimal control of population. *Journal of Chemical Physics*, 108(5):1953–1963, 1998.
- [9] Tommaso Caneva, Tommaso Calarco, and Simone Montangero. Chopped random-basis quantum optimization. *Physical Review A*, 84:022326, 2011.
- [10] Shai Machnes, Ulf Sander, Steffen J. Glaser, Pierre de Fouquières, Audrius Gruslys, Sophie Schirmer, and Thomas Schulte-Herbrüggen. Comparing, optimizing, and benchmarking quantum-control algorithms in a unifying programming framework. *Physical Review A*, 84:022305, 2011.
- [11] Pierre de Fouquières, Sophie Schirmer, Steffen J. Glaser, and Audrius Gruslys. Second order gradient ascent pulse engineering. *Journal of Magnetic Resonance*, 212(2):412–417, 2011.
- [12] Reuven Eitan, Michael Mundt, and David J. Tannor. Optimal control with accelerated convergence: Combining the Krotov and quasi-Newton methods. *Physical Review A*, 83:053426, 2011.
- [13] Ronnie Kosloff and Stuart A. Rice. Wavepacket dancing: Achieving chemical selectivity by shaping light pulses. *Journal of Chemical Physics*, 90(12):6947–6956, 1989.
- [14] Shuo Shi, Austin Woody, and Herschel Rabitz. Optimal control of selective vibrational excitation in harmonic linear chain molecules. *Journal of Chemical Physics*, 88(2):6870–6883, 1988.
- [15] János Somló, Vladimir A. Kazakov, and David J. Tannor. Controlled dissociation of I_2 via optical transitions between the X and B electronic states. *Chemical Physics*, 172(1):85–98, 1993.
- [16] Niels Rach, Markus M. Müller, Tommaso Calarco, and Simone Montangero. Dressing the chopped-random-basis optimization: A bandwidth-limited access to the trap-free landscape. *Physical Review A*, 92:062343, 2015.

- [17] Xun Luo, Pengfei Zhang, Victor V. Albert, and Liang Jiang. Quantum control under spectral constraints. *Physical Review A*, 98:042334, 2018.
- [18] Felix Motzoi, Jay M. Gambetta, Patrick Rebentrost, and Frank K. Wilhelm. Simple pulses for elimination of leakage in weakly nonlinear qubits. *Physical Review Letters*, 103:110501, 2009.
- [19] Robin Schutjens, Faris A. Dagga, Daniel J. Egger, and Frank K. Wilhelm. Single-qubit gates in frequency-crowded transmon systems. *Physical Review A*, 88:052330, 2013.
- [20] Volker Nebendahl, Hartmut Häffner, and Christian F. Roos. Optimal control of entangling operations for trapped-ion quantum computing. *Physical Review A*, 79:012312, 2009.
- [21] Markus M. Müller, Daniel M. Reich, Michael Murphy, Huan Yuan, Christiane P. Koch, K. Birgitta Whaley, and Tommaso Calarco. Optimizing entangling quantum gates for physical systems. *Physical Review A*, 84:042315, 2011.
- [22] Raj Chakrabarti and Herschel Rabitz. Quantum control landscapes. *International Reviews in Physical Chemistry*, 26(4):671–735, 2007.
- [23] Paolo Doria, Tommaso Calarco, and Simone Montangero. Optimal control technique for many-body quantum dynamics. *Physical Review Letters*, 106:190501, 2011.
- [24] Seth Lloyd and Simone Montangero. Information theoretical analysis of quantum optimal control. *Physical Review Letters*, 113:010502, 2014.
- [25] Michael H. Goerz, Daniel M. Reich, and Christiane P. Koch. Hybrid optimization schemes for quantum control. *EPJ Quantum Technology*, 2:21, 2015.
- [26] Daniel J. Egger and Frank K. Wilhelm. Adaptive hybrid optimal quantum control for imprecisely characterized systems. *Physical Review Letters*, 112:240503, 2014.
- [27] Julian Kelly, Rami Barends, Austin G. Fowler, Anthony Megrant, Evan Jeffrey, Theodore C. White, Daniel Sank, Josh Y. Mutus, B. Campbell, Yu Chen, Zijun Chen, Ben Chiaro, Andrew Dunsworth, Charles Neill, Peter J. J. O’Malley, Pedram Roushan, Ami Vainsencher, J. Wenner, Alexander N. Korotkov, Andrew N. Cleland, and John M. Martinis. Optimal quantum control using randomized benchmarking. *Physical Review Letters*, 112:240504, 2014.
- [28] Stephen Boyd, Neal Parikh, Eric Chu, Borja Peleato, and Jonathan Eckstein. Distributed optimization and statistical learning via the alternating direction method of multipliers. *Foundations and Trends in Machine Learning*, 3(1):1–122, 2011.
- [29] Neal Parikh and Stephen Boyd. Proximal algorithms. *Foundations and Trends in Optimization*, 1(3):127–239, 2014.

- [30] Jean-Jacques Moreau. Fonctions convexes duales et points proximaux dans un espace hilbertien. *Comptes Rendus de l'Académie des Sciences de Paris*, 255:2897–2899, 1962.
- [31] R. Tyrrell Rockafellar. Monotone operators and the proximal point algorithm. *SIAM Journal on Control and Optimization*, 14(5):877–898, 1976.
- [32] Magnus R. Hestenes. Multiplier and gradient methods. *Journal of Optimization Theory and Applications*, 4(5):303–320, 1969.
- [33] Roland Glowinski and Alain Marroco. Sur l'approximation, par éléments finis d'ordre un, et la résolution, par pénalisation-dualité, d'une classe de problèmes de Dirichlet non linéaires. *Revue Française d'Automatique, Informatique et Recherche Opérationnelle*, 9(R2):41–76, 1975.
- [34] Daniel Gabay and Bertrand Mercier. A dual algorithm for the solution of nonlinear variational problems via finite element approximation. *Computers and Mathematics with Applications*, 2(1):17–40, 1976.
- [35] Thomas Schulte-Herbrüggen, Alexander Spörl, Navin Khaneja, and Steffen J. Glaser. Optimal control-based efficient synthesis of building blocks of quantum algorithms: A perspective from network complexity towards time complexity. *Physical Review A*, 72:042331, 2005.
- [36] Shai Machnes, David J. Tannor, Frank K. Wilhelm, N. Katz, and Wolfgang Lechner. Tunable, flexible, and efficient optimization of control pulses for practical qubits. *Physical Review Letters*, 120:150401, 2018.
- [37] Michael H. Goerz, Felix Motzoi, K. Birgitta Whaley, and Christiane P. Koch. Charting the circuit QED design landscape using optimal control theory. *npj Quantum Information*, 3:37, 2017.
- [38] Amir Beck. *First-Order Methods in Optimization*. SIAM, 2017.
- [39] Jorge Nocedal and Stephen J. Wright. *Numerical Optimization*. Springer, 2 edition, 2006.
- [40] Dimitri P. Bertsekas. *Nonlinear Programming*. Athena Scientific, 2 edition, 1999.
- [41] C. G. Broyden. The convergence of a class of double-rank minimization algorithms. i. general considerations. *IMA Journal of Applied Mathematics*, 6(1):76–90, 1970.
- [42] Roger Fletcher. A new approach to variable metric algorithms. *Computer Journal*, 13(3):317–322, 1970.
- [43] Donald Goldfarb. A family of variable-metric methods derived by variational means. *Mathematics of Computation*, 24(109):23–26, 1970.

- [44] David F. Shanno. Conditioning of quasi-Newton methods for function minimization. *Mathematics of Computation*, 24(111):647–656, 1970.
- [45] Daoyi Dong and Ian R. Petersen. Quantum control theory and applications: A survey. *IET Control Theory and Applications*, 4(12):2651–2671, 2010.
- [46] Christiane P. Koch. Controlling open quantum systems: Tools, achievements, and limitations. *Journal of Physics: Condensed Matter*, 28(21):213001, 2016.
- [47] Daniel M. Reich, Moussa Ndong, and Christiane P. Koch. Monotonically convergent optimization in quantum control using Krotov’s method. *Journal of Chemical Physics*, 136:104103, 2012.
- [48] Michael H. Goerz, Daniel Basilewitsch, Fernando Gago-Encinas, Daniel J. Egger, Christiane P. Koch, and K. Birgitta Whaley. Krotov: A Python implementation of Krotov’s method for quantum optimal control. *SciPost Physics*, 7(6):080, 2019.
- [49] Steffen van Frank, Florian Wilhelm-Mauch, Andreas Schwarzkopf, Julius F. Schäff, Daniel Braukmann, Thomas Schweigler, Hartmut Häffner, and Jörg Schmiedmayer. Optimal control of complex atomic quantum systems. *Scientific Reports*, 6:34187, 2016.
- [50] Marin Bukov, Alexander G. R. Day, Dries Sels, Phillip Weinberg, Anatoli Polkovnikov, and Pankaj Mehta. Reinforcement learning in different phases of quantum control. *Physical Review X*, 8:031086, 2018.
- [51] M. López-Monjaraz et al. Impact of the π -pulse shape on the contrast of thermal atom interferometers. *Physical Review A*, 110:013109, 2024.